Geochimica et Cosmochimica Acta, Vol. 68, No. 23, pp. 4949–4962, 2004

0016-7037/04 $30.00 + .00

ELSEVIER

doi:10.1016/j.gca.2004.06.009

Constraints on clinopyroxene/melt partitioning of REE, Rb, Sr, Ti, Cr, Zr, and Nb during mantle melting: First insights from direct peridotite melting experiments at 1.0 GPa

A. Dana Johnston[1,*] and Brandon E. Schwab[2]

[1]Department of Geological Sciences, 1272 University of Oregon, Eugene, OR 97403, USA
[2]Department of Geology, Humboldt State University, Arcata, CA 95521, USA

(*Received December* 30, 2003; *accepted in revised form June* 4, 2004)

Abstract—Earlier piston-cylinder experiments in our laboratory produced a collection of mantle melting run products at 1.0 GPa that have now been analyzed by ion probe for selected REE, Ti, Cr, Rb, Sr, Y, Zr, and Nb. Natural starting materials were used and experiments were run in graphite-lined Pt capsules with the melt separated from the residual minerals into a layer of vitreous carbon spheres (VCS) to circumvent quench modification. The glass phase in 18 run products, representing melt percentages of ~2–20 wt%, yielded excellent data that were inverted to yield the first estimates ever of clinopyroxene/melt distribution coefficients, Ds, derived from direct peridotite partial melting experiments. Uncertainties were estimated with a Monte Carlo method.

For the REE and Y, these Ds were then compared to Ds calculated with the widely-used model of Wood and Blundy (1997) and the two sets overlap at the $\pm 2\sigma$ level in 123 of 128 cases (~96%). This indicates to us that: 1) the experiments analyzed here are well equilibrated with respect to major and trace element distributions, thus supporting the efficacy of the VCS technique and its variation involving diamond (e.g., Baker and Stolper, "Determining the composition of high-pressure mantle melts using diamond aggregates" [1994], *Geochim. Cosmochim. Acta* **58,** 2811–2827); 2) the model of Wood and Blundy (1997), calibrated largely on the basis of large melt fraction, inverse- or sandwich-type experiments, describes REE and Y partitioning during peridotite melting well, even very near the solidus; and it suggests that the cpx/melt Ds derived here for other elements, not modeled by the Wood and Blundy formulation, are probably also correct for peridotite melting to within their $\pm 2\sigma$ uncertainties. $D^{sp/liq}$ and $D^{cpx/liq}$ values for Cr calculated directly from electron microprobe data decrease by about a factor of five with increasing temperature and melt percentage.

The degree to which our experiments appear to have equilibrated seems at odds with recent measurements of the diffusivities of REE in diopside which suggest that relatively small percentages of our starting mineral grains should have equilibrated diffusively. Instead, we suggest that equilibration occurs much more rapidly through the processes of recrystallization and grain coarsening, accomplished through dissolution and reprecipitation. This suggestion is supported by the observation that our final grain sizes are typically 5–10 times larger than the ~10 μm starting sizes, indicating that substantial mass transfer occurred in our experiments, probably mediated by the melt phase in which diffusion is faster.

1. INTRODUCTION

Experimental studies of mantle melting at elevated pressure using natural peridotite starting materials have been pursued for nearly 40 years, since the pioneering efforts of O'Hara (1963) and Ito and Kennedy (1967) (see Kushiro, 2001, for a recent review). The primary goals of this work have been to determine the major element compositions of melts generated by partial fusion of peridotite and to evaluate how the compositions of the residual solids change with progressive melting. An important application of these data has been to gain insight into midocean ridge magmatism by comparing them to the compositions of erupted basaltic liquids at midocean ridges and abyssal peridotites which are interpreted to be residues of the melting process. While such studies are conceptually straight-forward, long experience has shown that high quality data are very difficult to obtain because of a host of technical difficulties that have compromised most previous attempts to some degree. Among these are uncertainties in the thermal profiles of the furnace assemblies, loss of Fe to noble metal capsules, inadvertent inclusion of adsorbed H_2O vapor in the starting rock powders, inadequate run durations to acceptably approach equilibrium and, perhaps most vexing, modification of the melt phase's composition during quenching of the experiments. But, since partial fusion of the mantle is so central to the geodynamics of the outer regions of our planet, efforts to continually improve both the experimental techniques employed, and the quality of the data gathered from the run products, have persisted to this day.

Workers in this field today employ well-characterized furnace assemblies (e.g., Pickering et al., 1998; Watson et al., 2002) and long ago developed techniques to minimize problems such as Fe-loss to Pt capsules and ingress of H_2O into nominally dry experimental charges. However, the critical problem of quench modification of melt compositions persisted and was only finally overcome with the development ten years ago of the diamond aggregate experimental technique (Baker et al., 1992; Hirose and Kushiro, 1992, 1993; Johnson and Kushiro, 1992; Baker and Stolper, 1994). This technique en-

* Author to whom correspondence should be addressed (adjohn@uoregon.edu).

ables physical separation of much of the melt phase from physical contact with residual crystals, so its composition is not affected by the development of overgrowths on these crystals during the experimental quench. As discussed early on by Jaques and Green (1979) and more recently by Baker and Stolper (1994; see in particular their fig. 2), development of quench overgrowths on residual peridotite mineral grains can lead to very large changes in the melt compositions (e.g., by factors of 2–3) by selective removal of some components from the melt with concomitant concentration of others. This problem is particularly severe in near-solidus experiments where the proportion of the original melt that is lost to the quench overgrowths is greatest. Such experiments are also of little value in studies of the behavior of trace elements both because of the quench modification problem and because typical melt (glass) pockets in such run products are substantially smaller than the smallest useful beam diameter obtainable with a magnetic sector ion probe or laser ablation ICP-MS leading to beam overlap onto adjacent crystals.

Earlier efforts to circumvent the quench modification problem (e.g., Stolper, 1980 and many others since) utilized so-called sandwich experiments in which a layer or plug of basaltic glass with a composition close to the suspected equilibrium composition at the run conditions is placed between layers of finely ground peridotitic minerals. The rationale is that the melt layer will equilibrate with the enclosing peridotite layers during the experiment and, because of its large dimensions, the composition of its central region will be relatively unaffected by the development of quench overgrowths on the peridotite minerals because they are physically far removed. This technique has several disadvantages over direct melting of peridotites, most notably the need to estimate accurately the equilibrium melt composition in advance of the experiment. If the estimated melt is too rich in clinopyroxene components, there is a tendency for cpx to crystallize along the crystal/melt interface effectively armoring it and hindering the melt's ability to equilibrate with the peridotite crystals. Robinson et al. (1998) employed an "iterative sandwich" technique to estimate the equilibrium melt composition, by continually adjusting the starting glass composition from one experiment to the next until it ceased changing. An additional disadvantage of sandwich-type experiments arising from their use of peridotite/basalt mixtures rather than peridotites alone, is that the observed melt fractions in any particular experiment are artificially elevated relative to those that would be produced from peridotites alone at the same conditions. In a similar vein, the bulk trace element contents of peridotite/basalt mixtures are much higher than in peridotites alone and thus such experiments do not accurately simulate the behavior of trace elements during mantle melting, although they do have the potential to provide good mineral/melt partitioning data (e.g., Salters et al., 2002; Gaetani et al., 2003; McDade et al., 2003). With the development of the diamond aggregate technique, it finally became possible to do melting experiments on peridotites with no added basalt and to obtain high quality major element melt compositions, even at very near-solidus temperatures (Baker et al., 1995). Although the technique had its detractors initially, careful subsequent tests of the technique (e.g., Wasylenski et al., 2003), and evaluation of the causes of conflicting data from other laboratories (e.g., Falloon et al., 2001), have resolved these initial concerns to most people's satisfaction. In this contribution, we extend this basic approach to study the behavior of selected trace elements during progressive partial melting of the mantle.

We utilized a variation on the diamond aggregate technique, in which vitreous carbon spheres were substituted for diamonds, in our previous experimental study of mantle melting at 1.0 GPa. This earlier work focused on five compositionally fertile peridotite starting materials with differing modes constructed from acid washed, hand-picked mineral separates from a fertile Kilbourne Hole xenolith (Pickering-Witter and Johnston, 2000) and another set of five modally equivalent, but compositionally intermediate starting materials constructed from minerals hand-picked from a compositionally intermediate xenolith from Mt. Noorat, Victoria, Australia. (Schwab and Johnston, 2001). Our experiments with each starting material covered the range in temperature from 1270 to 1390°C and generated melt fractions (F) from as small as 1.4 wt% to as large as 47.9 wt%; special emphasis was given to generating near-solidus melts. The major element compositions of all phases in all run products were determined by electron microprobe and modes were calculated by least-squares mass balance using these data in combination with the known bulk compositions of each starting material.

Here we report new ion microprobe measurements of selected trace element concentrations in the glass, representing melt percentages of 1.5–21.3 wt%, in run products produced from a subset of our starting materials. To our knowledge, these are the first such data to be presented from high pressure melting experiments using natural peridotite starting materials rather than peridotite/basalt mixtures. Thus, at near-solidus conditions, our melt fractions are low as they would be in the real mantle, and these run products provide an opportunity to assess the degree to which equilibrium trace element partitioning can be achieved in relatively cool, low melt fraction experiments using this relatively new experimental configuration. The principle goals of the study were: 1) to evaluate whether the trace element data support the conclusion reached previously from the major element data that these run products represent close approaches to equilibrium and thus good descriptions of mantle melting; 2) to evaluate whether the glass data set alone could be inverted to yield meaningful constraints on cpx/melt Ds; and 3) to explore whether our results can provide insight into the relative importance of mechanisms such as diffusion and dissolution/reprecipitation during experimental partial melting of multi-phase assemblages.

2. METHODS

2.1. Starting Materials

For this study we selected a subset of eighteen run products produced using compositionally intermediate modes INT-A, -B, and -E. The initial modes of these starting materials are tabulated in the upper part of Table 1 which has been reproduced from Schwab and Johnston (2001) for reader convenience. All contained 50 wt% olivine and 3% spinel, but differed in the relative abundances of the two pyroxenes. The A-mode approximates "average lherzolite" with opx $>$ cpx, the B-mode approximates wehrlite with cpx $\gg$ opx, and the E-mode splits the difference with cpx = opx. Our preferred major, minor, and trace element compositions of these materials are discussed after the experimental and analytical methods are presented.

Table 1. Starting material modes and compositions.

Mode	INT-A	INT-B	INT-E	Initial cpx	Initial opx
Ol	0.50	0.50	0.50	—	—
Opx	0.30	0.07	0.235	—	—
Cpx	0.17	0.40	0.235	—	—
Sp	0.03	0.03	0.03	—	—
		Major elements (wt %)			
SiO_2	46.19	45.65	46.04	53.91	56.22
TiO_2	0.04	0.04	0.04	m.d.l.	m.d.l.
Al_2O_3	2.58	2.60	2.59	3.10	3.02
Cr_2O_3	1.28	1.34	1.30	0.91	0.60
FeO[a]	6.85	6.11	6.64	2.29	5.55
MgO	38.43	34.64	37.35	17.32	33.88
CaO	4.00	8.87	5.39	21.96	0.78
MnO	0.12	0.10	0.11	0.07	0.13
Na_2O	0.10	0.21	0.13	0.53	0.03
K_2O	0.05	0.04	0.05	n.a.	n.a.
P_2O_5	0.01	0.01	0.01	n.a.	n.a.
NiO	0.21	0.21	0.21	m.d.l.	m.d.l.
Total	99.86	99.82	99.86	100.09	100.21
Mg#[b]	90.9	91.0	90.9	93.1	91.6
Cr#[c]	24.9	25.8	25.2	16.4	11.8
		Trace elements (ppm)			
La	2.08	3.64	2.56	9.33	0.02
Ce	2.69	3.61	2.98	5.38	0.03
Nd	0.92	1.04	0.97	1.05	0.01
Sm	0.17	0.19	0.18	0.21	0.01
Dy	0.14	0.17	0.15	0.17	0.01
Er	0.09	0.13	0.10	0.21	0.01
Yb	0.12	0.17	0.13	0.27	0.05
Ti	222	222	222	178	78
Cr	8758	9168	8895	4442	2700
Rb	3.14	2.79	3.04	n.a.	n.a.
Sr	11.15	23.21	14.84	55.20	0.62
Y	0.79	1.08	0.87	1.89	0.14
Zr	3.41	3.26	3.23	1.58	0.31
Nb	1.16	1.57	1.29	2.10	0.17

Note. INT-A,-B,-E: major elements by microprobe combined with modes apart from TiO_2, K_2O, and P_2O_5 which were analyzed by ICP-ES; trace elements by ICP-MS; Cr by microprobe combined with modes.

Initial cpx and opx major elements: average of 20 microprobe analyses (n.a. = not analyzed; m.d.l. = less than minimum detectable limit; 0.02 wt %); trace elements: average of seven ion probe analyses of each (N. Shimizu, analyst).

[a] All Fe reported as FeO.

[b] Molar (Mg/(Mg + Fe)) ×100.

[c] Molar (Cr/(Cr + Al)) ×100.

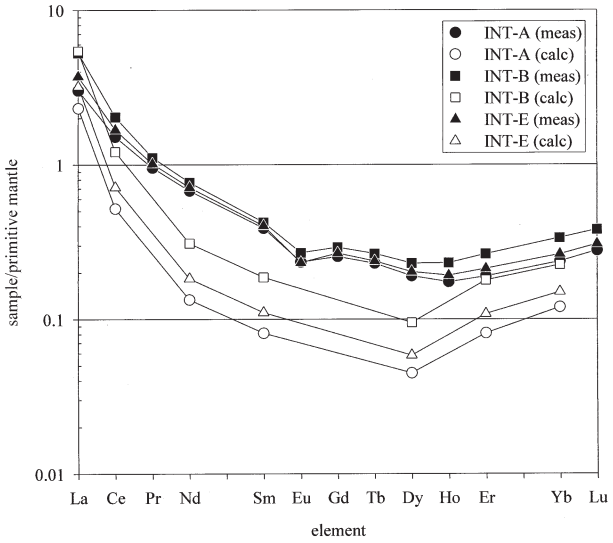

Fig. 1. REE patterns of our starting materials normalized to Sun and McDonough's (1989) estimate of the primitive mantle. Solid symbols show ICP-MS data from the same powders that were used in the experiments. Open symbols show patterns calculated from ion probe analyses of the interiors of hand-picked cpx and opx grains taken from the separates that were used to construct the starting materials together with their modal abundances, assuming that olivine and spinel contain zero REE. Although the patterns agree within estimated 2σ uncertainties for La and Yb (20 and 40% relative, respectively), the ICP-MS data indicate 2 to 5 times higher concentrations of all other REE suggesting that these "excess" REE are concentrated in grain rims or reside along grain boundaries and thus were missed in the ion probe analyses. The ICP-MS data are taken as correct. Only selected REE were analyzed by ion probe.

2.2. Experimental

Experiments were performed in 1/2 inch (1.27 cm) end-loaded solid-medium piston-cylinder apparatus with CaF_2/MgO/graphite-based furnace assemblies as described by Pickering et al. (1998). Considerable care was exercised to ensure that the thermocouple and capsule were located within the furnace hot spot, defined as that region that does not vary by more than 10°C from the peak temperature. Sample position was carefully measured before and after each experiment. Samples were encapsulated in graphite-lined Pt 'ash cans' (Sneeringer and Watson, 1985) 3.5 mm in diameter and ~5 mm tall. A layer of vitreous carbon spheres, 80–100 μm in diameter, was loaded above the peridotite powder and acted as a melt sink. After loading the capsules they were stored open at 120°C for at least several hours before welding the lids on while still hot in an attempt to minimize the ingress of H_2O vapor in the air into the charges.

The wetting properties of the vitreous carbon spheres draw the melt into these layers during the experiments. As discussed in detail by Schwab and Johnston (2001) these melts communicate via diffusion with melts interstitial to peridotite mineral grains in the lower portion of the capsules and, if run durations are sufficient, the melt among the spheres acquires the equilibrium composition, despite being physically separated from the solid peridotite material. The melt among the spheres quenches to crystal-free glass rinds on the spheres (see fig. 1 of Schwab and Johnston, 2001 for a SEM photomicrograph), several to tens of microns thick, upon termination of the experiments. As documented in Table 2, experimental durations ranged from 2 to 3 days at the highest temperatures to 3–5 days at the lower temperatures. Pickering-Witter and Johnston (2000) and Schwab and Johnston (2001) devoted considerable discussion to evaluating the approach to equilibrium of these experiments and concluded, based on major element data, that these run durations were more than sufficient to achieve time-invariant melt compositions and homogeneous olivine and spinel grains, but they also noted that some unreacted pyroxene cores, accounting for <10% of the total pyroxene, remained. The olivine/melt Fe-Mg distribution coefficients tabulated in Table 2 (0.34 ±0.01; 1σ) also support a close approach to equilibrium in all of the experiments considered here. The behavior of selected trace elements during these experiments is documented here and provides another opportunity to assess the experiments' approach to equilibrium.

2.3. Analytical

The major element compositions of the bulk starting materials were estimated from their known modes and electron microprobe analyses of their constituent minerals (see Schwab and Johnston, 2001 for details) and were cross-checked and supplemented with analyses for major and minor elements by solution ICP-ES. These latter data, and trace element analyses by solution ICP-MS, were measured in dissolved aliquots of the same powders that were used in the experiments. Trace element abundances in the glasses reported on here, as well as the hand-picked starting cpx and opx grains used to construct the starting

Table 2. Run conditions and calculated modes (wt %).

Run	T (°C)	Duration (h)	Gl	Ol	Cpx	Opx	Sp	$K^{ol/liq}$[a]
INT-A4	1390	48	21.3 (6)	53.6 (9)		24.6 (1.3)	0.5 (1)	0.35 (2)
INT-A5	1360	72	17.4 (6)	53.0 (8)		28.6 (1.0)	1.0 (1)	0.35 (1)
INT-A3	1330	72	12.2 (5)	55.4 (7)	10.7 (8)	21.3 (1.0)	0.5 (0)	0.35 (2)
INT-A13	1315	120	6.9 (5)	53.7 (8)	13.4 (9)	25.0 (1.4)	1.0 (1)	0.34 (1)
INT-A8	1300	97.5	3.3 (4)	51.9 (1.3)	15.9 (1.5)	27.5 (2.0)	1.4 (2)	0.34 (1)
INT-A12	1285	96	2.9 (4)	52.9 (1.2)	15.6 (1.6)	27.0 (2.0)	1.7 (2)	0.35 (2)
INT-B4	1390	48	19.5 (8)	51.7 (5)	28.8 (1.1)			0.34 (2)
INT-B8	1380	72	19.5 (5)	51.1 (4)	29.4 (7)			0.34 (2)
INT-B12	1360	119.5	12.5 (6)	51.4 (6)	35.7 (8)		0.5 (1)	0.34 (2)
INT-B11	1345	103	6.3 (6)	50.7 (6)	42.4 (9)		0.6 (1)	0.33 (2)
INT-B6	1330	73	5.4 (9)	51.7 (9)	41.8 (1.5)		1.1 (3)	0.33 (2)
INT-B10	1310	126	3.6 (6)	51.0 (8)	44.1 (1.1)		1.3 (2)	0.34 (1)
INT-B7	1290	142	2.2 (7)	50.9 (9)	45.3 (1.3)		1.6 (3)	0.37 (2)
INT-E5	1390	65	20.1 (5)	51.3 (7)	27.9 (1.0)		0.7 (1)	0.34 (1)
INT-E7	1360	93.5	12.5 (4)	54.5 (1.0)	32.5 (1.9)	0.0 (2.3)	0.6 (1)	0.34 (2)
INT-E6	1345	116	7.2 (6)	56.7 (1.3)	30.7 (2.1)	4.6 (2.7)	0.8 (1)	0.35 (2)
INT-E3	1330	93	4.4 (5)	57.1 (1.3)	30.6 (9)	6.6 (1.9)	1.3 (1)	0.33 (1)
INT-E1	1300	120	1.5 (4)	55.6 (1.2)	29.3 (8)	11.9 (1.7)	1.8 (1)	0.33 (2)

Note. Numbers in parentheses are 1σ errors propagated from the 1σ errors on the analyzed phase compositions and the bulk compositions. Errors given in terms of least unit cited (e.g., 21.3 (6) = 21.3 ±0.6).

[a] $K^{ol/l} = (X_{Fe}/X_{Mg})^{ol}/(X_{Fe}/X_{Mg})^{liq}$. From Schwab and Johnston (2001) for reader convenience.

materials, were measured by ion microprobe (SIMS). The analyses of the starting cpx and opx allowed us to calculate expected REE concentrations in our bulk starting materials (assuming ol and sp to contain zero REE) which we could then compare to the measured REE analyses by ICP-MS.

2.3.1. ICP-ES and -MS Analyses

These analyses were performed in the geochemistry laboratory in the Department of Earth Sciences at Boston University, directed by Dr. T. Plank. An important goal was to obtain high quality REE analyses, so a protocol involving sample digestion in $HF:HNO_3$ mixtures in Savillex screw-top vials was employed. Sample preparation and instrumental procedures followed those reported in Kelley et al. (2003) except a final dilution of 1/1500, rather than the 1/2000 used for basalts, was used because of the low trace element abundances of peridotites. Samples were calibrated externally, using basalt standard reference materials (K1919, MAR, JB-3) that were spiked with Mg to match the peridotite matrix. Each sample was measured in duplicate, with an average standard deviation of 2% relative for the trace elements measured by ICP-MS and 1% for the major and minor elements measured by ICP-ES. For the purpose of calculating uncertainties on the derived cpx trace element Ds presented later in this contribution, somewhat generous 1σ uncertainties of 5% relative were assigned to all ICP-MS trace element data. An unfortunate consequence of the sample digestion method employed is that silica was volatilized and little of the Cr-spinel dissolved; steps taken to account for these problems are outlined below.

2.3.2. Ion Probe Analyses

These data were collected using the Cameca IMS-3f SIMS at the Northeast Regional Ion Microprobe Facility at Woods Hole Oceanographic Institution, directed by Dr. N. Shimizu. A primary O^- beam with a current of 0.7 nA, an energy of 12.47 kV, and a diameter of 10–12 μm was focused on Au-coated samples. A 60 V offset was employed for the REE analyses whereas a 90 V offset was used for the other trace elements reported. Unfortunately, with a 60 V offset, the peaks for the analyzed Eu and Ba isotopes overlap leading to apparent Eu concentrations that are too high. Accordingly, Eu data have been excluded from the tables and figures that follow. The instrument was calibrated each day using either clinopyroxene standard KH-1 (Irving and Frey, 1984) or glass standard KL2-G (Jochum et al., 2000).

The glass rinds on the vitreous carbon spheres were quite easily located despite the poor optics of the instrument because of the polishing relief that developed due to their differing hardnesses. However, the rinds were often too thin to fully contain the primary ion beam and, in these instances, overlap with the carbon spheres was unavoidable. However, many samples contained thick rinds that could be easily analyzed with no such overlap and these analyses were indistinguishable from other analyses from the same samples, collected from thinner rinds for which overlap could not be avoided. This indicates that the spheres contained neither detectable Si nor trace elements and that the analytical routine, which normalizes the trace element data to Si contents, resulted in this overlap having no effect apart from decreasing the total trace element and Si counts, but leaving their ratio ~ constant. Thus, while the counts were lower and the errors were higher on overlapped analyses, the values were much the same as on analyses from spots with no overlap.

Each spot analysis in fact consisted of five separate ion counting intervals and, based on the variability of these intraanalysis results, the estimated 1σ uncertainties on the glass analyses are 10% relative for La, Ce, and Ti; 15% relative for Nd, Sr, and Zr; 20% relative for Sm, Dy, Er, Yb, and Y; and 30% relative for Rb, and Nb. These relatively large uncertainties result from both the low analyzed concentrations and the small beam diameter (~11 μm) and low beam current employed. The data in Table 3 generally represent averages of two to five different spot analyses, taken from among the glass rinds surrounding the carbon spheres or sometimes, in the case of high-*F* experiments, from the upper portions of glass pools, far from gravitationally settled crystals, as well (in these cases the rind and pool analyses were indistinguishable). Exceptions are the REE data from INT-E3 and the other trace element data from INT-B10 which represent only one spot analysis each. Average uncertainties for all elements, estimated from the range in spot analyses from each sample, are smaller (about two-thirds) than the uncertainties estimated from intra-analysis variability quoted earlier and listed in the footnote of Table 3. These larger uncertainties are used in all calculations that follow.

2.4. Preferred Starting Material Compositions

2.4.1. Major and Minor Elements

In Table 1 we tabulate our preferred major, minor, and trace element compositions of the three starting materials studied here as well as the starting cpx and opx grains hand-picked from the Mt. Noorat spinel lherzolite xenolith. As noted above, the dissolution method employed

Table 3. Ion microprobe analyses of experimental glasses (ppm).

Sample	T(°C)	dur(hr)	F(wt. %)	La	Ce	Nd	Sm	Dy	Er	Yb	Ti	Cr	Rb	Sr	Y	Zr	Nb
INT-A bulk[a]			100.0[b]	2.08	2.69	0.92	0.17	0.14	0.09	0.12	222	8758	3.14	11.15	0.79	3.41	1.16
INT-A4	1390	48	21.3	7.8	10.2	2.6	0.8	0.4	0.3	0.4	795	5689	6	45.6	2.6	13.6	4
INT-A5	1360	72	17.4	9.7	14.3	4.3	1.3	0.6	0.5	0.5	860	4239	8	53.7	3.6	20.4	6
INT-A3	1330	72	12.2	12.1	15.7	4.7	1.2	0.6	0.5	0.5	914	6992	7	74.6	3.9	19.2	6
INT-A13	1325	120	6.9	19.7	27.0	7.6	1.5	1.0	0.8	0.6	1242	4470	11	87.2	4.4	19.0	5
INT-A8	1300	97.5	3.3	33.2	48.1	12.3	2.9	1.3	0.7	0.9	1367	2545	15	144.7	4.7	45.6	18
INT-A12	1285	96	2.9	40.3	52.8	12.9	2.4	1.1	0.7	0.7	1790	1699	26	200.7	7.0	69.2	26
INT-B bulk[a]			100.0[b]	3.64	3.61	1.04	0.19	0.17	0.13	0.17	222	9168	2.79	23.21	1.08	3.26	1.57
INT-B4	1390	48	19.5	13.0	14.7	3.6	0.8	0.5	0.4	0.4	735	7083	3	90.0	3.9	14.4	7
INT-B8	1380	72	19.5	12.4	14.4	3.8	0.9	0.6	0.4	0.4	694	6929	5	84.5	3.8	14.3	6
INT-B12	1360	119.5	12.5	18.1	19.9	5.4	0.9	0.5	0.5	0.5	813	6193	7	110.5	4.9	21.1	8
INT-B11	1345	103	6.3	26.9	28.1	6.1	1.1	0.7	0.6	0.6	960	4350	8	159.6	4.5	35.1	13
INT-B6	1330	73	5.4	34.0	38.0	8.6	1.6	1.1	0.4	0.5	1481	3655	9	232.1	6.0	39.9	22
INT-B10	1310	126	3.6	50.6	51.2	9.7	1.7	1.0	0.7	0.6	1483	2233	15	286.6	5.7	51.7	22
INT-B7	1290	142	2.2	49.7	50.9	10.0	1.7	1.0	0.5	0.5	1577	1597	17	272.8	6.2	49.8	41
INT-E bulk[a]			100.0[b]	2.56	2.98	0.97	0.18	0.15	0.10	0.13	222	8895	3.04	14.84	0.87	3.23	1.29
INT-E5	1390	65	20.1	8.4	11.1	3.2	0.6	0.5	0.4	0.4	769	6174	6	50.3	3.3	13.1	5
INT-E7	1360	93.5	12.5	11.7	15.0	3.9	0.8	0.6	0.4	0.3	1339	6514	15	96.1	4.4	45.6	11
INT-E6	1345	116	7.2	20.5	26.2	7.0	1.4	0.9	0.5	0.5	1039	4108	13	95.3	4.2	24.2	11
INT-E3	1330	93	4.4	33.8	44.7	9.9	2.2	0.9	1.0	0.8	1659	2554	18	116.9	3.6	37.1	10
INT-E1	1300	120	1.5	50.5	65.3	12.4	2.5	1.2	0.7	0.6	1604	1977	33	258.1	7.5	66.1	28

[a] Data for bulk samples measured by ICP-MS or electron microprobe (Cr), from Table 1.
[b] Melt % set to 100% for bulk samples.

Note. Estimated 1σ uncertainties from SIMS intra-analysis statistics (see text): 10% relative: La, Ce, Ti, Cr; 15%: Nd, Sr, Zr; 20%: Sm, Dy, Er, Yb, Y; 30%: Rb, Nb. Data generally represent averages of two to five spot analyses on each run product and uncertainties based on this variability are less (~2/3) than those quoted above for all elements.

for the ICP-MS and -ES analyses resulted in only partial dissolution of the 3% Cr-spinel in each analyzed powder, leading to analyses that are deficient in components contained in this phase (i.e., Cr_2O_3,Al_2O_3, FeO, and MgO), and volatilization of silica required that it be calculated by difference. Because of these complications, we have adopted instead (Table 1) the bulk major element compositions calculated from the starting modes and mineral compositions (by microprobe). These compositions were also used by Schwab and Johnston (2001) in their mass-balance calculations of the modes of these run products, values that are used in trace element mass balance calculations presented later in this contribution. We have supplemented the analyses reproduced from Schwab and Johnston (2001) for INT-A, -B and -E in Table 1 with ICP-ES data for K_2O, P_2O_5, and TiO_2 and note that these concentrations, together with the ICP-MS trace element data discussed below, are relative to the initial weight of the sample, containing all of the Cr-spinel, and so are true concentrations of the analyzed powders despite the fact that much of the spinel did not actually dissolve. The FeO, MgO, CaO, Al_2O_3, and Na_2O contents determined by the two methods agree within 10% relative.

2.4.2. Trace Elements

The trace and minor element data reported for INT-A, -B, and -E in the lower portion of Table 1 were all measured by ICP-MS apart from the Cr values which were calculated from the modes of the starting materials and electron probe analyses of Cr in the starting minerals. We believe Cr to be the only reported trace or minor element in these starting material analyses to be compromised by the incomplete dissolution of Cr-spinel. For example, the TiO_2 abundance in the starting spinel is quite low (~0.03 wt%; Schwab and Johnston, 2001) and thus it could contribute only ~5 ppm Ti to the bulk starting materials (of which sp accounts for only 3 wt%), far less than the ~220 ppm Ti measured by ICP-MS. Zr and Nb were likely also little-affected judging from their very low $D^{sp/cpx}$ distribution coefficients, estimated from analyses of coexisting minerals in natural xenoliths (~0.001 and 0.01, respectively; Eggins et al., 1998). Averaged spot ion probe analyses for trace elements in the starting pyroxenes also appear in Table 1 and, considering the measured Zr and Nb concentrations in the cpx, the low $D^{sp/cpx}$ distribution coefficients cited above, and the fact that spinel accounts for only 3% of the bulk starting materials, it is unlikely that spinel could account for even 0.1% of the Zr and Nb measured in the bulk starting materials by ICP-MS.

In Figure 1 we show with filled symbols the REE patterns of our three starting materials normalized to Sun and McDonough's (1989) estimate of primitive mantle. These patterns are distinctly LREE-enriched with normalized La values of ~3–5 and normalized MREE and HREE values in the range 0.7 to 0.2. This degree of depletion of the MREE and HREE (relative to primitive mantle) accords with the depletion also observed in the incompatible major elements (e.g., Na, Ti, Al) and suggests that the mantle volume represented by the xenolith from which these starting materials were prepared had lost a melt component earlier in its history. However, the striking LREE-enrichment appears to require that this mantle region was subsequently refertilized metasomatically before the eruption that brought this xenolith to the surface. Evidence for such a multi-stage history is quite commonly seen in the trace element geochemistry of mantle xenoliths (e.g., Frey and Green, 1974; McDonough and Frey, 1989; Eggins et al., 1998). Apparently, metasomatism had the effect of increasing the concentrations of LREE without much affecting the MREE, HREE, or major incompatible elements. Regardless of the details of the process, the net effect of metasomatism was to substantially elevate the abundances of the LREE, thus easing our task of analyzing for them.

2.4.3. Comparison with Calculated REE Abundances

Before beginning this study, multiple grains from the cpx and opx mineral separates prepared from the Mt. Noorat xenolith were mounted and analyzed by ion probe for REE. With these data (Table 1) and the initial modes of the starting materials, we calculated the expected bulk REE concentrations in our three starting materials, assuming that olivine and spinel contain zero REE and we show these values, also normalized to primitive mantle (Sun and McDonough, 1989), with open symbols on Figure 1. To our surprise, the bulk REE abundances estimated in this way deviate significantly from the concentrations measured by solution ICP-MS. For the three INT modes, the La and Yb data agree within estimated 2σ uncertainties (20 and 40% relative, respectively) but all other REEs have concentrations 2 to 5 times higher in the ICP-MS data compared to the calculated values, with the mis-

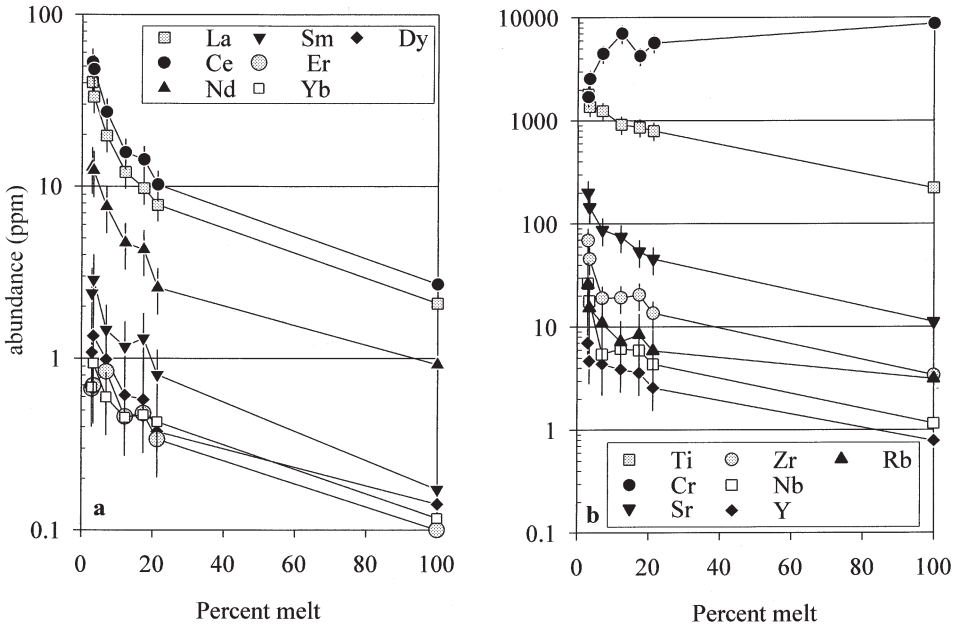

Fig. 2. Representative plots showing the variation of selected trace elements in the glass phase with percent melt. a) REE in run products produced with starting material INT-A; b) other trace elements in the same run products. The values plotted at 100% melt represent the bulk starting composition (Table 1). Vertical error bars represent estimated $\pm 2\sigma$ uncertainties. Uncertainties on the melt fractions are smaller than the symbols.

match increasing systematically from both ends, and peaking at Sm and Nd. Interestingly, the agreement between the two approaches is best for the B-mode, then the E-mode and finally, the A-mode, the same order in which the abundance of cpx decreases and opx increases. The ICP-MS data appear to require a repository of REE in our bulk starting materials other than cpx and opx. However, since no "exotic" phase (e.g., apatite, amphibole, glass) was observed in thin sections of the starting xenolith we surmise that the "extra" REEs were added to cpx and opx rims metasomatically but went undetected in our ion probe analyses of grain mounts of the starting pyroxenes which focused on grain interiors. Alternatively, these "extra" REE might reside on grain boundaries within the xenolith (e.g., Hiraga et al., 2003, 2004). While we do not know with certainty the cause of these mismatches, we have nonetheless adopted the ICP-MS data as representative of our starting bulk trace element concentrations, apart from Cr which was calculated from microprobe data as described above. We are comfortable with this conclusion because the ICP-MS data were collected on dissolved aliquots of the same finely ground powders that were used in the experiments, and because standards analyzed in parallel with our samples recovered accepted concentrations.

3. RESULTS

Our ion probe analyses of the glass in 18 run products are summarized in Table 3, together with run temperatures, durations, and melt percentages calculated by major element mass balance. The first row in each section gives the trace element concentrations of the bulk starting material (set equal to 100% melt) measured as described above. The ion probe data appear beneath this with the experiments arranged in order of decreasing melt percentage. Thus, in scanning from the top to bottom of each section, calculated melt percentages decrease from 100% to as low as 1.5% in our near-solidus runs.

The data in Table 3 show that the trace elements behaved as one would expect with decreasing melt fraction, indicating a close approach to equilibrium in these experiments. For example, for each starting material there are marked increases in the REE concentrations as melt fractions decrease, reflecting their incompatible behavior with respect to mantle minerals. And, at any particular melt fraction, the enrichment in LREE relative to the bulk starting materials is greater than for HREE reflecting the relatively greater incompatibility of LREE, and, as expected, this effect is enhanced at lower melt fractions. The incompatible behaviors of Ti, Rb, Sr, Y, Zr, and Nb are also apparent from their increasing concentrations with decreasing melt fraction, while the opposite behavior is observed for Cr, which behaves compatibly with respect to the mantle mineral assemblage.

Representative plots (for INT-A) illustrating this behavior are shown in Figures 2a and b where element concentrations are plotted against melt percentage, calculated from major element mass balance. The patterns on these plots are generally smooth although small anomalies do occasionally appear. The most extreme example of the 18 run products considered here is run INT-A5, appearing at 17.4% melt in Figures 2a and b, where the concentrations of most incompatible elements appear somewhat enriched, and compatible Cr appears depleted, relative to the runs on either side of it. Even these rare, relatively large discrepancies are within the estimated uncertainties on the ion probe measurements quoted in the footnote to Table 3. For example, the apparent small positive anomalies for Ce, Nd, Sm, Er, Yb, Dy, Zr, Rb, Nb, and Y at 17.5% melt disappear completely or switch sign if the measured concentrations are lowered within the uncertainty bounds quoted in Table 3, and the negative anomaly at Cr is very substantially damped if its concentration is increased within its estimated uncertainty. However, we note that in this particular instance all incompatible elements deviate from the overall trend in the same direction, perhaps indicating a minor problem with this experiment

(e.g., temperature uncertainty), although its melt fraction seems about right relative to those in the next hottest and coolest runs.

4. DISCUSSION

4.1. Constraints on $D^{cpx/liq}$ Values

The primary goal of this study was to determine mineral/melt distribution coefficients, $D^{xtl/liq}$, appropriate for mantle melting at 1.0 GPa by measuring them in the direct peridotite partial melting experiments discussed here. However, despite obtaining high quality data from the glass phase in each run product, similar data could not be obtained from the crystalline phases because of their small sizes (in low-F runs) or, more commonly, their extremely low concentrations of trace elements. Accordingly, we resorted instead to an indirect method of constraining the $D^{xtl/liq}$ values based on mass balance, and narrowed our focus to cpx alone as it vastly dominates the behavior of the trace elements discussed here during mantle melting, apart perhaps from Cr which we discuss separately.

4.1.1. Calculation of $D^{cpx/liq}$ Values

Trace element mass balance in experiments like ours is described by the batch melting equation (Shaw, 1970):

$$C_L/C_o = 1/[\bar{D} + F(1 - \bar{D})], \quad (1)$$

where F is the melt fraction, C_L is the concentration of the trace element in the liquid, C_o is its concentration in the bulk starting material, and $\bar{D}$ is its bulk solid/liquid distribution coefficient, formulated from the individual mineral/melt distribution coefficients, $D^{xtl/liq}$s, weighted according to their mass fractions of the melt-free solid residue, X^{xtl}:

$$\bar{D} = X^{ol}D^{ol/liq} + X^{opx}D^{opx/liq} + X^{cpx}D^{cpx/liq} + X^{sp}D^{sp/liq}. \quad (2)$$

Recognizing that each of the X^{xtl}s above can also be described as $W^{xtl}/(1 - F)$ where W^{xtl} is the weight fraction of the mineral in the full, melt-bearing run product normalized by the fraction of total solid in the run product, $(1 - F)$, Eqn. 2 may be recast as:

$$\bar{D} = [W^{ol}D^{ol/liq} + W^{opx}D^{opx/liq} + W^{cpx}D^{cpx/liq} + W^{sp}D^{sp/liq}]/(1 - F). \quad (3)$$

Finally, combining Eqns. 1 with 3 and rearranging yields the following expression for the distribution coefficient of some trace element between cpx and coexisting melt:

$$D^{cpx/liq} = [C_o/C_L - W^{ol}D^{ol/liq} - W^{opx}D^{opx/liq} - W^{sp}D^{sp/liq} - F]/W^{cpx} \quad (4)$$

From Eqn. 4 we see that a value for $D^{cpx/liq}$ can be calculated for each analyzed trace element in each cpx-bearing run product using the data in Table 1 (C_o), Table 2 (W^{xtl} and F), and Table 3 (C_L), provided values for $D^{ol/liq}$, $D^{opx/liq}$, and $D^{sp/liq}$ can be specified.

The values we used for this purpose are tabulated in Table 4 and derive in large part from compilations of $D^{xtl/liq}$s assembled by Kelemen et al. (1993) and Halliday et al. (1995); other sources appear in the table footnotes. The adopted values lie within the range of experimentally determined $D^{xtl/liq}$ values compiled, for example, on the Geochemical Earth Reference Model (GERM) web page (http://www.earthref.org/). While one could debate the relative merits of any particular value, the important point, as we will show, is that virtually every element considered in Table 4 is so much more incompatible in ol, opx, and sp than in cpx that our detailed choices of $D^{xtl/liq}$ make little difference to the resulting $D^{cpx/liq}$ values. Our calculated $D^{cpx/liq}$ values for all analyzed elements but Cr, which we discuss separately, are tabulated in Table 5. Before discussing these results, it is important that we first evaluate their uncertainties, particularly given their very derivative nature and the large number of variables involved in their calculation.

Table 4. Mineral/melt distribution coefficients used in calculations of $D^{cpx/liq}$.

Element	$D^{ol/liq}$	$D^{opx/liq}$	$D^{sp/liq}$
La	0.000007[a]	0.0005[a]	0.0006[a]
Ce	0.00001[a]	0.0009[a]	0.0006[a]
Nd	0.00007[a]	0.009[a]	0.0006[a]
Sm	0.0007[a]	0.02[a]	0.0006[a]
Dy	0.004[a]	0.06[a]	0.0015[a]
Er	0.009[a]	0.07[a]	0.003[a]
Yb	0.023[a]	0.1[a]	0.0045[a]
Y	0.0082[b]	0.015[b]	0.0006[c]
Ti	0.015[b]	0.086[b]	0.300[d]
Rb	0.0003[b]	0.0002[b]	0.00096[c]
Sr	0.0004[b]	0.0007[b]	0.000004[c]
Zr	0.001[b]	0.012[b]	0.00108[c]
Nb	0.00005[b]	0.003[b]	0.00065[c]

[a] From compilation by Kelemen et al. (1993).
[b] From compilation by Halliday et al. (1995).
[c] Calculated from $D^{sp/cpx}$ values from Eggins et al. (1998, Table 4; laser ablation data from cpx-bearing harzburgite) combined with $D^{cpx/liq}$ values from Halliday et al. (1995).
[d] Average $D^{sp/liq}_{Ti}$ calculated from electron probe data in all sp-bearing INT runs (Schwab and Johnston, 2001; range: 0.14–0.54).

4.1.2. Uncertainties on Calculated $D^{cpx/liq}$ values

From Eqn. 4 it is apparent that each of our calculated $D^{cpx/liq}$ values is a function of ten variables, each with its own associated uncertainty. To evaluate the interplay of these variables and arrive at estimates of the uncertainties on our calculated $D^{cpx/liq}$ values we employed a Monte Carlo procedure. In detail, we specified the mean (i.e., measured or adopted value) and one standard deviation (i.e., uncertainty) for each variable, and had a random generator generate a population of 5000 numbers representing a full (i.e., $\pm$multiple σ), normal distribution about the specified mean and with the specified variance. Our use of 5000 numbers ensured that the mean and 1σ of the list so generated matched those specified at the outset to within at least 0.5% relative. After generating such lists for each of the ten variables, Eqn. 4 was then solved 5000 times using values for the ten variables from successive rows, and the mean of this population of solutions was taken as $D^{cpx/liq}$ and its standard deviation was taken as the 1σ uncertainty on this calculated $D^{cpx/liq}$ value.

To proceed, we had to first assign 1σ uncertainties to each of the ten variables in Eqn. 4. For the modal data, F, W^{ol}, W^{opx}, W^{sp}, and W^{cpx}, we used the 1σ uncertainties reported in Table

Table 5. Derived cpx/melt D's with associated 1 σ uncertainties estimated by Monte Carlo methods.

Run	T (°C)	F (%)	La	Ce	Nd	Sm	Dy	Er	Yb	Y	Ti	Rb	Sr	Zr	Nb
IA-3	1330	12.2	0.48 (0.17)	0.47 (0.17)	0.72 (0.33)	0.27 (0.37)	0.99 (0.63)	0.64 (0.57)	1.09 (0.78)	0.79 (0.53)	0.90 (0.38)	3.36 (11.36)	0.29 (0.24)	0.54 (0.30)	0.75 (7.61)
IA-13	1315	6.9	0.28 (0.10)	0.23 (0.10)	0.39 (0.18)	0.37 (0.26)	0.48 (0.35)	0.17 (0.30)	0.75 (0.52)	0.84 (0.39)	0.60 (0.28)	1.85 (5.80)	0.46 (0.18)	0.83 (0.27)	1.24 (3.82)
IA-8	1300	3.3	0.19 (0.07)	0.15 (0.06)	0.26 (0.12)	0.16 (0.14)	0.37 (0.26)	0.52 (0.33)	0.39 (0.36)	0.87 (0.36)	0.61 (0.27)	1.23 (3.89)	0.29 (0.11)	0.26 (0.12)	0.24 (1.29)
IA-12	1285	2.9	0.15 (0.06)	0.15 (0.06)	0.2 (0.12)	0.27 (0.17)	0.59 (0.33)	0.60 (0.36)	0.75 (0.47)	0.53 (0.26)	0.40 (0.24)	0.68 (2.81)	0.18 (0.09)	0.12 (0.09)	0.12 (0.93)
IB-4	1390	19.5	0.31 (0.15)	0.19 (0.13)	0.37 (0.22)	0.14 (0.23)	0.63 (0.38)	0.58 (0.37)	0.67 (0.41)	0.31 (0.29)	0.35 (0.11)	2.42 (5.80)	0.24 (0.14)	0.12 (0.12)	0.16 (1.89)
IB-8	1380	19.5	0.35 (0.14)	0.20 (0.12)	0.29 (0.19)	0.10 (0.20)	0.35 (0.28)	0.50 (0.46)	0.72 (0.40)	0.34 (0.28)	0.40 (0.10)	1.24 (7.20)	0.29 (0.13)	0.12 (0.11)	0.32 (2.14)
IB-12	1360	12.5	0.22 (0.09)	0.17 (0.08)	0.21 (0.12)	0.29 (0.18)	0.71 (0.42)	0.38 (0.30)	0.65 (0.42)	0.29 (0.19)	0.39 (0.08)	0.88 (2.85)	0.25 (0.09)	0.09 (0.07)	0.22 (1.04)
IB-11	1345	6.3	0.17 (0.05)	0.16 (0.05)	0.26 (0.09)	0.27 (0.12)	0.42 (0.16)	0.38 (0.16)	0.52 (0.20)	0.44 (0.17)	0.38 (0.06)	0.70 (2.20)	0.20 (0.06)	0.07 (0.04)	0.17 (0.65)
IB-6	1330	5.4	0.13 (0.05)	0.10 (0.05)	0.17 (0.08)	0.17 (0.10)	0.26 (0.13)	0.62 (0.23)	0.62 (0.24)	0.31 (0.15)	0.21 (0.06)	0.68 (1.61)	0.12 (0.05)	0.07 (0.05)	0.06 (0.43)
IB-10	1310	3.6	0.08 (0.02)	0.08 (0.02)	0.17 (0.05)	0.18 (0.07)	0.33 (0.10)	0.35 (0.10)	0.54 (0.14)	0.35 (0.10)	0.23 (0.04)	0.38 (0.85)	0.11 (0.03)	0.06 (0.02)	0.09 (0.33)
IB-7	1290	2.2	0.12 (0.02)	0.11 (0.02)	0.18 (0.02)	0.20 (0.05)	0.36 (0.08)	0.50 (0.11)	0.65 (0.14)	0.34 (0.08)	0.24 (0.05)	0.35 (0.91)	0.14 (0.04)	0.10 (0.04)	0.05 (0.11)
IE-5	1390	20.1	0.38 (0.09)	0.25 (0.08)	0.39 (0.16)	0.50 (0.26)	0.34 (0.23)	0.20 (0.20)	0.43 (0.27)	0.26 (0.22)	0.29 (0.10)	1.14 (5.01)	0.36 (0.15)	0.18 (0.13)	0.35 (2.49)
IE-7	1360	12.5	0.30 (0.07)	0.23 (0.06)	0.39 (0.12)	0.30 (0.16)	0.47 (0.21)	0.40 (0.19)	0.86 (0.32)	0.23 (0.15)	0.10 (0.06)	0.30 (1.59)	0.10 (0.07)	−0.16 (0.03)	0.00 (0.80)
IE-6	1345	7.2	0.18 (0.05)	0.14 (0.05)	0.23 (0.09)	0.20 (0.12)	0.30 (0.16)	0.41 (0.19)	0.68 (0.28)	0.45 (0.19)	0.42 (0.12)	0.60 (2.30)	0.29 (0.10)	0.21 (0.09)	0.17 (0.89)
IE-3	1330	4.4	0.11 (0.03)	0.08 (0.03)	0.18 (0.06)	0.12 (0.07)	0.38 (0.14)	0.16 (0.10)	0.31 (0.15)	0.65 (0.20)	0.24 (0.08)	0.45 (1.25)	0.28 (0.07)	0.14 (0.06)	0.29 (1.16)
IE-1	1300	1.5	0.12 (0.03)	0.10 (0.01)	0.22 (0.05)	0.19 (0.07)	0.37 (0.12)	0.41 (0.14)	0.58 (0.20)	0.34 (0.11)	0.34 (0.09)	0.29 (0.77)	0.15 (0.04)	0.11 (0.04)	0.12 (0.33)

2 which were calculated by the method of Albarede and Provost (1977) by propagating 1σ uncertainties on the electron microprobe analyses, assessed from multiple analyses of each phase, through the least-squares modal mass balance calculations. These uncertainties are typically <5% relative but can be substantially larger for phases in low abundance. Uncertainties of 50% relative (1σ) were arbitrarily assigned to the adopted values for $D^{ol/liq}$, $D^{opx/liq}$, and $D^{sp/liq}$ although we note that a choice of 25% or 75% has no discernible impact on the calculated $D^{cpx/liq}$ values. The same can be said of their estimated uncertainties apart from the least incompatible elements in the experiments with the lowest melt fractions, but even these variations are relatively small with, for example, the uncertainty on Yb in run INT-A12 (2.9% melt) changing by only ~13% relative, as the uncertainties on the D values for ol, opx, and sp are varied within the range specified above. Finally, 1σ uncertainties of 5% relative were assigned to all the C_o values measured by ICP-MS and the 1σ uncertainties on the C_L values measured by ion probe are as summarized in the footnote to Table 3. With these estimated uncertainties on the input variables we estimated the 1σ uncertainty on each of the 13 $D^{cpx/liq}$ values calculated for each of the 16 cpx-bearing run products and tabulate these values in parentheses in Table 5, together with their associated $D^{cpx/liq}$ values. The magnitudes of these uncertainties primarily reflect the magnitudes of the uncertainties assigned to the ion probe analyses. However, fairly large uncertainties occasionally arise even for elements for which the ion probe uncertainty is rather small (e.g., INT-A3 at 12.2% melt) and these correspond to run products with relatively low modal abundances of cpx.

4.1.3. Discussion of $D^{cpx/liq}$ Values

The $D^{cpx/liq}$ estimates tabulated in Table 5 are plotted against melt percentage in Figure 3 for all elements except Rb and Nb for which the estimated uncertainties are so large (commonly hundreds of percent) that the plots would be of little value. We chose to show only the $\pm 1\sigma$ uncertainty bounds (68% of the variance) on this figure to keep it a manageable size but show the more inclusive (95% of the variance) $\pm 2\sigma$ bounds in subsequent figures (e.g., Figs. 4, 5, and 6).

Inspection of Figure 3 fails to reveal any compelling systematic variations in the $D^{cpx/liq}$ values with increasing melt fraction although the 2σ uncertainties (twice the magnitude of the error bars shown) would certainly allow them. Indeed, we have every reason to expect significant variation in the $D^{cpx/liq}$ values since the major element compositions of both the cpx and melt vary significantly among the run products considered (see Schwab and Johnston, 2001, Table 4). Earlier work (e.g., McKay et al., 1986; McKay, 1989; Hack et al., 1994; Gaetani and Grove, 1995; Blundy et al., 1998; Hill et al., 2000; Salters et al. 2002) has demonstrated strong dependencies of $D^{cpx/liq}$ on major element phase compositions, particularly the CaO content of the cpx and the Al_2O_3 contents of both the cpx and melt. Among our run products, cpx CaO and Al_2O_3 abundances range from 6.4–19.3 wt% and 1.8–5.1 wt%, respectively, and melt Al_2O_3 contents range from 9.7–17.4 wt%. Thus, while we expect variations in the $D^{cpx/liq}$ values represented by our experiments, we conclude that they are not resolvable given our uncertainties.

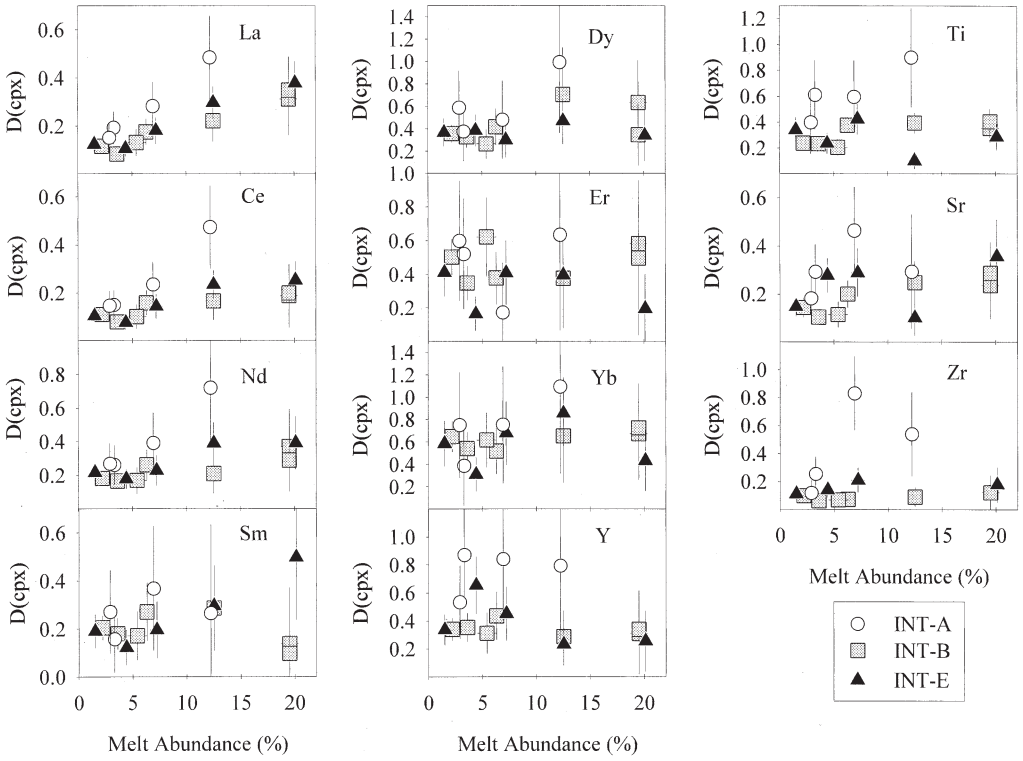

Fig. 3. $D^{cpx/liq}$ values, calculated as described in the text, vs. percent melt. Note that just $\pm 1\sigma$ uncertainties are shown here and the lower bound of some of these have been truncated at 0.0 since negative $D^{cpx/liq}$ values have no meaning. The upper bounds have also been truncated in a few instances (Nd, Dy, Er, Yb, and Y for INT-A and Sm for INT-E). Also, note that the Zr value for IE-7 (-0.16 ± 0.03, 1σ, Table 5) does not appear on the plot because it is negative, and that similar plots for Nb and Rb are not shown since the estimated uncertainties on these calculated $D^{cpx/liq}$ values are so large (Table 5).

4.2. Comparision of Calculated $D^{cpx/liq}$ Values with the Wood and Blundy (1997) Model

As an alternative means of evaluating the variability of our estimated $D^{cpx/liq}$ values as a function of melt fraction and thus phase composition, we chose to compare them with values calculated by the widely-used model of Wood and Blundy (1997). This model describes cpx/melt partitioning for REE and Y and assigns principle control to the properties of the cpx, particularly the mismatch between cation size and the dimensions of its crystallographic site, and the associated strain energy. It parameterizes $D^{cpx/liq}$ values as a function of experimental P and T, cpx major element composition, and melt *Mg#* (molar Mg/(Mg + Fe)) and is calibrated with 454 experimental observations from the literature. The authors state that their model returns the experimental values to within a factor of 0.6–1.7 in 92% (i.e., $\sim 2\sigma$) of the 454 cases. That is, the $\sim \pm 2\sigma$ variance of model values spans from -40% to $+70\%$ relative and we have approximated this by assigning 1σ uncertainties of 30% of the calculated values.

In Table 6 we tabulate the $D^{cpx/liq}$ values calculated by the Wood and Blundy (1997) model for each of our 16 cpx-bearing experiments. For any particular run product the Ds increase from LREE to HREE by factors of 5–10, whereas for any particular element in a particular starting material, we see systematic increases by factors of 1.3–2.6 with decreasing melt fraction. In Figure 4 we show this comparison graphically by plotting the ratio of our calculated Ds to the corresponding Ds calculated with the Wood and Blundy (1997) model vs. melt fraction. The horizontal line at 1.0 represents perfect agreement. We calculated the relative uncertainties on these ratios as the square root of the sum of the squares of the relative uncertainties estimated by the Monte Carlo procedures described earlier (Table 5) and the 30% relative errors assigned to the Wood and Blundy (1997) calculations. Absolute 1σ uncertainties are obtained by multiplying these values by the value of the ratio. The actual error bars plotted on Figure 4 represent $\pm 2\sigma$ bounds but many of their lower extensions have been truncated at 0.0 since negative D values have no physical meaning.

From Figure 4 it is clear that the $D^{cpx/liq}$ values estimated here agree with those calculated with the model of Wood and Blundy (1997) in virtually all cases. In detail, once the $\pm 2\sigma$ uncertainty bounds on the ratios plotted in Figure 4 are considered, it is permissible that our estimated $D^{cpx/liq}$ values agree with those calculated with the Wood and Blundy (1997) model in 123 of 128 cases, or 96% of the time; those few points that miss, barely do so. We thus conclude that our $D^{cpx/liq}$ values, estimated from direct peridotite partial melting experiments, agree with those in the Wood and Blundy (1997) calibrating database, despite the fact that the latter largely derive from

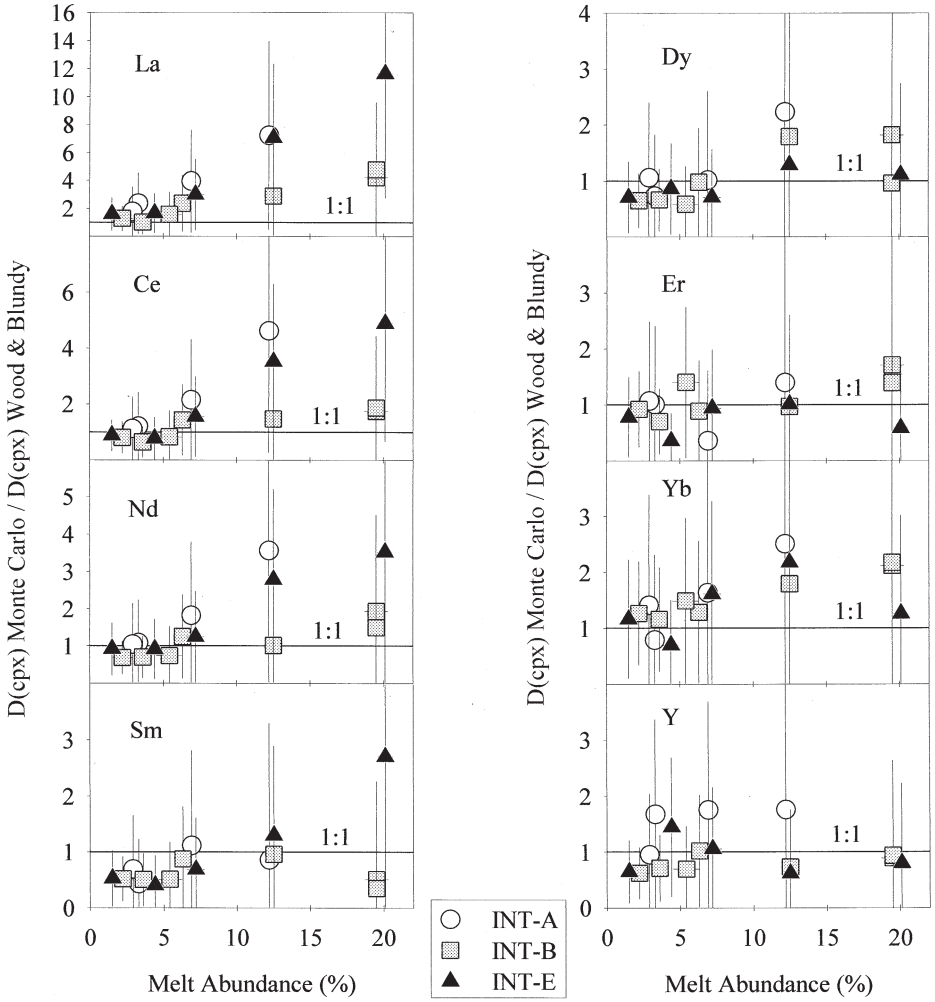

Fig. 4. Ratios of the $D^{cpx/liq}$ values calculated here with those calculated with the model of Wood and Blundy (1997) plotted vs. percent melt. The error bars shown represent $\pm 2\sigma$ errors propagated though the ratio calculation and many have their lower extensions truncated at 0.0. The horizontal line at 1.0 represents perfect agreement; 96% of the points agree within the shown uncertainties.

inverse experiments with basalts and peridotite/basalt sandwich-type experiments, neither of which utilize peridotite bulk compositions. This lends considerable support to: 1) the suitability of the Wood and Blundy model for modeling REE and Y partitioning during mantle melting at 1.0 GPa; 2) the notion that our experiments equilibrated to a very substantial degree; and 3) the likelihood that the $D^{cpx/liq}$ values estimated here for the other trace elements (i.e., Ti, Cr, Rb, Sr, Zr, and Nb), not modeled by the Wood and Blundy formulation, are also appropriate for mantle melting at 1.0 GPa within their stated $\pm 2\sigma$ uncertainty bounds. These conclusions are further supported by the forward modeling results presented below.

4.3. Forward Modeling of C_L Values

Another way to appreciate the good agreement between our calculated $D^{cpx/liq}$ values and those returned by the Wood and Blundy (1997) model is to compare our REE and Y ion probe measurements with C_L values calculated using the model $D^{cpx/liq}$ values. Rearranging Eqn. 4 to solve for C_L yields:

$$C_L = C_o/[W^{ol}D^{ol/liq} + W^{opx}D^{opx/liq} + W^{cpx}D^{cpx/liq} + W^{sp}D^{sp/liq} + F] \quad (5)$$

Using C_o values from Table 1, W^{xtl} and F values from Table 2, model $D^{cpx/liq}$ values from Table 6, and values for the other $D^{xtl/liq}$s from Table 4, we calculated the expected abundances of REE and Y in the glass in 18 of our run products, including two that lack cpx (INT-A4, -A5), for a total of 144 results.

We show our results graphically in Figure 5 where we plot the measured abundances (horizontally) vs. those calculated as described above. The uncertainties assigned to the measurements are as summarized in the footnote to Table 3 and those on the calculated C_L values were estimated by the same Monte Carlo procedures described earlier but by solving Eqn. 5 5000 times rather than Eqn. 4. The diagonal solid lines represent perfect agreement and the error bars shown are $\pm 2\sigma$ bounds. Each plot summarizes the results from all experiments with a particular starting material, with each experiment shown with a different symbol type. For example, five different symbol types

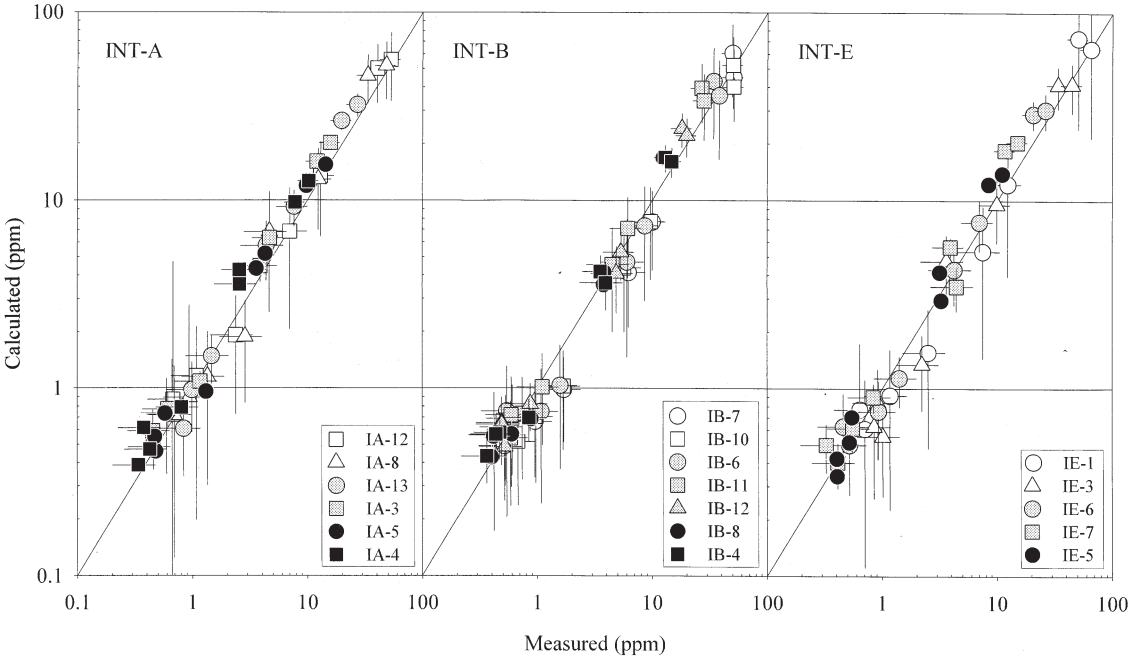

Fig. 5. Concentrations of REE and Y calculated as described in the text plotted vs. the ion probe measurements. The error bars shown represent $\pm 2\sigma$ uncertainties and the diagonal lines with slopes of 1.0 represent perfect agreement. Note that the calculated values incorporate $D^{cpx/liq}$ values from the Wood and Blundy (1997) model. Greater than 96% of points agree once the uncertainties are considered.

appear in the first panel of Figure 5 (for INT-A), one for each of the five experiments run with starting material INT-A, and each of these symbol types appears eight times on the plot, each point representing a different analyzed REE or Y in that particular run. Points plotting at the largest values represent the LREE in the lowest-*F* experiments whereas those at the lowest

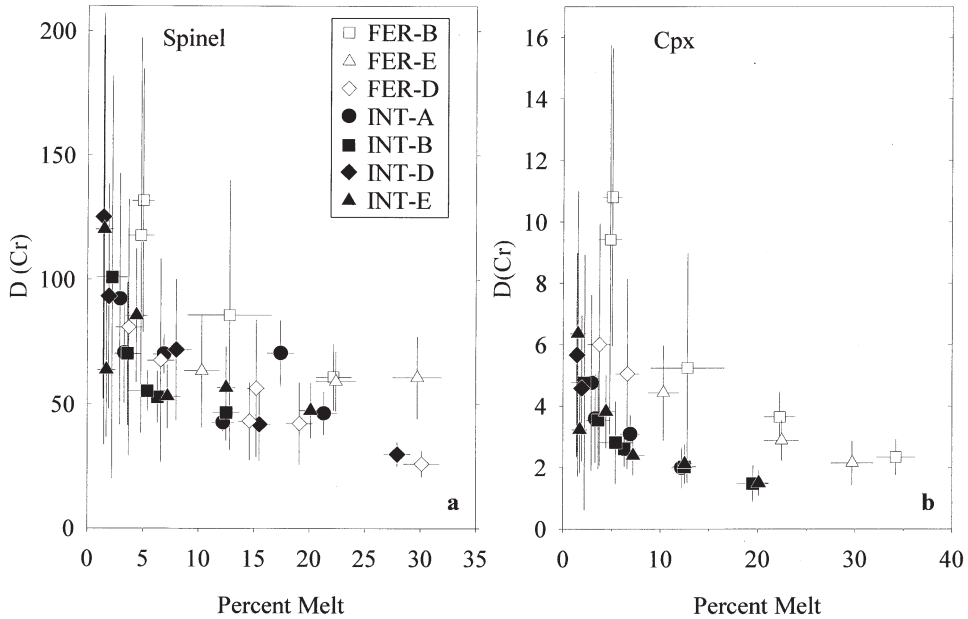

Fig. 6. $D^{sp/liq}$ and $D^{cpx/liq}$ values for Cr (calculated from electron microprobe data) vs. percent melt. In addition to the three starting materials discussed previously, this plot also includes data for starting material INT-D from Schwab and Johnston (2001) and FER-B, FER-D, and FER-E from Pickering-Witter and Johnston (2000). Error bars are estimated 2σ uncertainties propagated through the ratio calculation. Although the detailed behavior of each starting material differs, the $D^{sp/liq}$ and $D^{cpx/liq}$ values clearly decrease with increasing melt percentage and temperature.

Table 6. Cpx/Melt REE and Y Ds calculated with the model of Wood and Blundy (1997).[a]

	T (°C)	F (%)	La	Ce	Nd	Sm	Dy	Er	Yb	Y
INT-A3	1330	12.2	0.07	0.10	0.20	0.31	0.45	0.46	0.44	0.45
INT-A13	1315	6.9	0.07	0.11	0.22	0.33	0.47	0.48	0.46	0.48
INT-A8	1300	3.3	0.08	0.12	0.24	0.37	0.51	0.52	0.49	0.52
INT-A12	1285	2.9	0.09	0.13	0.26	0.39	0.55	0.56	0.53	0.56
INT-B4	1390	19.5	0.07	0.11	0.19	0.27	0.35	0.34	0.32	0.35
INT-B8	1380	19.5	0.07	0.11	0.19	0.28	0.36	0.36	0.33	0.36
INT-B12	1360	12.5	0.08	0.11	0.21	0.30	0.39	0.39	0.36	0.40
INT-B11	1345	6.3	0.07	0.11	0.21	0.31	0.43	0.43	0.40	0.43
INT-B6	1330	5.4	0.08	0.12	0.23	0.34	0.45	0.44	0.41	0.45
INT-B10	1310	3.6	0.08	0.12	0.24	0.36	0.49	0.49	0.47	0.50
INT-B7	1290	2.2	0.09	0.14	0.27	0.40	0.55	0.54	0.51	0.55
INT-E5	1390	20.1	0.03	0.05	0.11	0.18	0.31	0.34	0.34	0.32
INT-E7	1360	12.5	0.04	0.07	0.14	0.23	0.37	0.39	0.39	0.38
INT-E6	1345	7.2	0.06	0.09	0.18	0.28	0.42	0.43	0.42	0.43
INT-E3	1330	4.4	0.06	0.10	0.20	0.30	0.44	0.46	0.44	0.45
INT-E1	1300	1.5	0.08	0.12	0.24	0.36	0.52	0.53	0.50	0.53

[a] Calculated using major element cpx and melt compositions from Schwab and Johnston (2001) and the model of Wood and Blundy (1997). Runs INT-A4 and INT-A5 do not appear here because they lack cpx.

values represent the HREE in the highest-F experiments. From Figure 5 it is clear that the agreement between our ion probe measurements and our calculations employing $D^{cpx/liq}$ values from the Wood and Blundy (1997) model is excellent, with 138 of the 144 measurements (96%) matching the calculations at the $\pm 2\sigma$ level.

4.4. Behavior of Cr

We chose to treat Cr separately as it is the only minor element of those we analyzed that behaves compatibly with respect to the mantle assemblage and because its solid/liquid partitioning behavior is controlled dominantly by Cr-spinel rather than cpx as is the case for all other analyzed elements. Although we did analyze the glass in the run products discussed here for Cr by ion probe (Table 3) we have no similar data from the cpx or spinel. Accordingly, we opted to use electron microprobe data instead because we have such data for the glass, cpx, and spinel in all of the run products discussed here (from Schwab and Johnston, 2001) and thus can calculate $D^{sp/liq}$ and $D^{cpx/liq}$ values for Cr directly, without mixing data types. This choice also allows us to include in our analysis cpx- and/or sp-bearing run products from the study by Schwab and Johnston (2001) that were not analyzed by ion probe, as well as examples from the study by Pickering-Witter and Johnston (2000), for a total of 29 $D^{cpx/liq}$ and 35 $D^{sp/liq}$ determinations.

An interesting observation from Figure 2 is that the Cr concentration of the glass in our run products increases markedly over the first ~10% melting in contrast to the near-constant, buffered concentrations expected theoretically for a compatible element with a near-constant and large $\bar{D}$. This requires that the $\bar{D}$ for Cr decrease with increasing melt fraction in our experiments, due either to decreasing modal abundances of spinel and cpx, the principle controls on Cr partitioning, or decreasing $D^{sp/liq}$ and/or $D^{cpx/liq}$ values. The run product modes reported by Schwab and Johnston (2001) and Pickering-Witter and Johnston (2000) show that the modal abundances of both phases do indeed decrease with increasing melt fraction, but Figures 6a and b show that decreasing $D^{sp/liq}$ and $D^{cpx/liq}$ values also play a role. Although the detailed behavior of each starting material differs, they collectively exhibit variations in $D^{sp/liq}$ from near-solidus values of ~70–130 to values as low as ~25–60 at ~30% melting. The $D^{cpx/liq}$ values track these variations with near-solidus values of 6–11, decreasing to ~2 after ~35% melting. The error bars shown represent $\pm 2\sigma$ uncertainties propagated through the ratio calculation and these generally decrease with increasing melt fraction reflecting the increasingly Cr-rich compositions of higher temperature spinels and, to a lesser degree cpx too, and thus the smaller relative errors on the Cr analyses. Comparison of our ranges of $D^{sp/liq}$ and $D^{cpx/liq}$ values with previous experimental determinations in basaltic systems (Geochemical Earth Reference Model (GERM) web page (http://www.earthref.org/)) demonstrates that our range of the former encompasses the few previous determinations in the literature whereas the literature range of the latter encompasses the values we determined. However, in neither case is the melt fraction-, or temperature dependence of these Ds as clearly shown as in Figure 6. Clearly, $D^{sp/liq}$ and $D^{cpx/liq}$ are functions of mineral and melt composition but developing a detailed understanding of these dependencies is beyond the scope of this contribution.

4.5. Comparison with Diffusion Studies

The results presented above provide compelling evidence that the experiments reported on here equilibrated with respect to both major and trace elements to an impressive degree and it is therefore of interest to compare our observations with the results of diffusion studies to try to gain some understanding of the mechanism by which experiments like ours equilibrate. Experimental measurements of the temperature-dependent diffusivities of selected REE in diopside were recently reported by Van Orman et al. (2001). Using data from their Table 5 we calculated diffusion coefficients, D, for La and Yb, at 1270°C and 1390°C, the temperature range covered in our experiments: $D_{La,1270C} = 10^{-19.99} m^2/s$; $D_{La,1390C} = 10^{-18.86} m^2/s$; $D_{Yb,1270C} = 10^{-18.55} m^2/s$; and $D_{Yb,1390C} = 10^{-17.55} m^2/s$. These were then used to estimate diffusion length scales, L, in

our experiments using the approximation $L = (Dt)^{1/2}$ where t is the run duration in seconds. Using 100 hours as a typical run duration at 1270°C, we calculate values for $L_{La,1270C}$ and $L_{Yb,1270C}$ of 0.06 μm and 0.16 μm respectively, far smaller than the ~10 μm grain size of our starting powders. By comparison, using 50 hours as typical for 1390°C runs, we calculate values for $L_{La,1390C}$ and $L_{Yb,1390C}$ of 0.32 μm and 0.71 μm, approximately five times greater than at 1270°C but still far short of our starting grain radii. Finally, to estimate the fraction of our starting grains that would be expected to equilibrate with the melt via diffusion, we approximated them as spheres with diameters of 10 μm and calculated the vol.% of such grains that outer shells with the thicknesses derived above would account for. This exercise yielded values ranging from as little as 3.5% for slow-diffusing La at 1270°C, to as much as 36.9% for faster-diffusing Yb at 1390°C. These results, particularly for the LREE, suggest that little of our residual cpx should have equilibrated with the melt if diffusion was the operative mechanism.

The discrepancy between our observations and the expectations resulting from our rough diffusion calculations quite clearly indicates that diffusion is not the first-order mechanism by which our run products approached equilibrium. Instead, we speculate that equilibration is largely accomplished through a dissolution/reprecipitation mechanism wherein cpx grains partially to fully dissolve in disequilibrium proportions early in the experiments and adjust with time to the equilibrium abundance for the run conditions via reprecipitation from the melt onto remaining cpx substrates. This inference is supported by the observation that our final grain sizes are typically 5–10 times larger than at the start of the experiments. Such very large textural changes require significant mass transfer and we infer that the process by which this was accomplished facilitated equilibration of our experiments. If correct, this would account for the dominance of very large grains in our run products. And, since the bulk of the cpx is in the outer portions of these large crystals, which clearly represent new growth from the melt in which diffusion is fast, it would be expected that the experiments would equilibrate to a much greater degree than by bulk diffusion through cpx alone.

5. SUMMARY AND CONCLUSIONS

In this contribution we present ion probe analyses for selected REE and Ti, Cr, Rb, Sr, Y, Zr, and Nb in the glass phase in 18 high pressure (1.0 GPa) experimental run products generated in batch partial melting experiments involving three different peridotitic starting materials. Aliquots of the same bulk powdered starting materials were analyzed for the same trace elements by ICP-MS and for major elements by ICP-ES. Electron microprobe analyses of the major element compositions of all phases in each run product enabled calculation of their modes, including melt fraction, by least-squares inversion. Thus, for each run product we know well the melt fraction, *F*, the mode of the residual crystalline assemblage, the starting bulk trace element concentrations (C_o), and the C_L values determined for each element by ion probe. Combining this information with individual mineral/melt distribution coefficients for olivine, orthopyroxene, and spinel from the literature enabled us to calculate $D^{cpx/liq}$ values for each cpx-bearing run product via the batch melting mass-balance equation. For the REE and Y, these values agree with those calculated by the model of Wood and Blundy (1997) 96% of the time when estimated $\pm 2\sigma$ uncertainties are considered. This very good agreement between the calculations and measurements supports the conclusion reached earlier by Pickering-Witter and Johnston (2000) and Schwab and Johnston (2001) that these run products approached equilibrium very closely and thus provide good descriptions of batch melting of compositionally and mineralogically variable mantle at 1.0 GPa. This also supports the notion that the Ds determined for the other trace elements that are not modeled by the Wood and Blundy (1997) formulation are also appropriate for mantle melting at 1.0 GPa once their uncertainties are considered. However, this conclusion is at odds with recent measurements of the REE diffusivities in diopside which suggest that very little of our starting cpx should have equilibrated diffusively given our 2–5 d run durations. This, combined with our observation that the grain sizes in our run products are 5–10 times larger than our average starting grain size, lead us to speculate that equilibrium is instead approached via a dissolution/reprecipitation and grain coarsening mechanism with the melt phase, in which diffusion is fast, mediating the process.

Acknowledgments—We are very grateful for the hospitality and guidance of Dr. Nobu Shimizu, Dr. Graham Layne, and Mr. Pete Landry of the Northeast Regional Ion Microprobe Facility without whose help this work would not have been possible. We also thank Dr. Terry Plank for facilitating the ICP-MS and -ES analyses and for her insightful comments on an earlier version of this paper. Michael Shaffer's assistance with electron microprobe analyses is gratefully acknowledged as is the help of Kate Wearn and Julie Roberge in preparing SEM maps in advance of the ion probe work. We are particularly grateful to Dr. Michael Baker for more than can be listed here, including two thorough and critical reviews of earlier versions of this paper that led to very substantial improvements. Drs. Jon Blundy, Glenn Gaetani, and Maik Pertermann also contributed official reviews that led to substantial improvements. Dr. Fred Frey's efforts as the associate editor handling this contribution are also much-appreciated. The experimental run products that form the basis of this contribution were prepared with funding from the National Science Foundation (EAR-9506045, EAR-9804913) and the ion probe work reported here was funded by NSF-EAR-0105500.

Associate editor: F. Frey

REFERENCES

Albarede F. and Provost A. (1977) Petrological and geochemical mass-balance equations: An algorithm for least-squares fitting and general error analysis. *Comp. Geosci.* **3,** 309–326.

Baker M. B., Newman S., Beckett J. R., and Stolper E. M. (1992) Separating liquid from crystals in high-pressure melting experiments using diamond aggregates (abstract). *Geol. Soc. Am. Abstr. Prog.* **24,** A256.

Baker M. B. and Stolper E. M. (1994) Determining the composition of high-pressure mantle melts using diamond aggregates. *Geochim. Cosmochim. Acta* **58,** 2811–2827.

Baker M. B., Hirschmann M. M., Ghiorso M. S., and Stolper E. M. (1995) Compositions of near-solidus peridotite melts from experiments and thermodynamic calculations. *Nature* **375,** 308–311.

Blundy J. D., Robinson J. A. C., and Wood B. J. (1998) Heavy REE are compatible in clinopyroxene on the spinel lherzolite solidus. *Earth Planet. Sci. Lett.* **160,** 493–504.

Eggins S. M., Rudnick R. L., and McDonough W. F. (1998) The composition of peridotites and their minerals: A laser-ablation ICP-MS study. *Earth Planet. Sci. Lett.* **154,** 53–71.

Falloon T. J., Danyushevsky L. V., and Green D. H. (2001) Peridotite melting at 1 GPa: Reversal experiments on partial melt compositions produced by peridotite-basalt sandwich experiments. *J. Petrol.* **42,** 2363–2390.

Frey F. A. and Green D. H. (1974) The mineralogy, geochemistry and origin of lherzolite inclusions in Victorian basanites. *Geochim. Cosmochim. Acta* **38,** 1023–1059.

Gaetani G. A. and Grove T. L. (1995) Partitioning of rare earth elements between clinopyroxene and silicate melt: Crystal-chemical controls. *Geochim. Cosmochim. Acta* **59,** 1951–1962.

Gaetani G. A., Kent A. J. R., Grove T. L., Hutcheon I. D., and Stolper E. M. (2003) Mineral/melt partitioning of trace elements during hydrous peridotite partial melting. *Contrib. Mineral. Petrol.* **145,** 391–405.

Hack P. J., Nielsen R. L., and Johnston A. D. (1994) Experimentally-determined rare-earth and Y partitioning behavior between clinopyroxene and basaltic liquids at pressures up to 20 kbar. *Chem. Geol.* **117,** 89–106.

Halliday A. N., Lee D-C, Tommasini S., Davies G. R., Paslick C. R., Fitton J. G., and James D. E. (1995) Incompatible trace elements in OIB and MORB and source enrichment in the sub-arc mantle. *Earth Planet. Sci. Lett.* **133,** 79–395.

Hill E., Wood B. J., and Blundy J. D. (2000) The effect of Ca-Tschermaks component on trace element partitioning between clinopyroxene and silicate melt. *Lithos* **53,** 203–215.

Hiraga T., Anderson I. M., and Kohlstedt D. L. (2003) Chemistry of grain boundaries in mantle rocks. *Am. Mineral.* **88,** 1015–1019.

Hiraga T., Anderson I. M., and Kohlstedt D. L. (2004) Grain boundaries as reservoirs of incompatible elements in the Earth's mantle. *Nature* **427,** 699–703.

Hirose K. and Kushiro I. (1992) Partial melting of dry peridotites at high pressure: Determination of compositions of melts segregated from peridotite using aggregates of diamond (abstract). *EOS* **73**, 615.

Hirose K. and Kushiro I. (1993) Partial melting of dry peridotites at high pressures: Determination of compositions of melts separated from peridotite using aggregates of diamonds. *Earth. Planet. Sci. Lett.* **114,** 477–489.

Irving A. J. and Frey F. A. (1984) Trace element abundances in magacrysts and their host basalts: Constraints on partition coefficients and megacryst genesis. *Geochim. Cosmochim. Acta* **48,** 1201–1221.

Ito K. and Kennedy G. C. (1967) Melting and phase relations in a natural peridotite to 40 kbar. *Am. J. Sci.* **265,** 519–538.

Jaques A. L. and Green D. H. (1979) Determination of liquid compositions in experimental high pressure melting of peridotites. *Am. Mineral.* **64,** 1312–1321.

Jochum K. P., Dingwell D. B., Rocholl A., Stoll B., Hofmann A. W., Becker S., Besmehn A., Bessette D., Dietz H-J, Dulski P., Erzinger J., McDonough W. F., Maetz M., Mezger K., Munker C., Nikogosian I. K., Pickhardt C., Raczek I., Rhede D., Seufert H. M., Simakin S. G., Sobolov A. V., Spettel B., Straub S., Vincze L., Wallianos G., Weyer S., Wolf D., and Zimmer M. (2000) The preparation and preliminary characterization of eight geochemical MPI-DING reference glasses for in-situ microanalysis. *Geostand. Newslett.* **24,** 87–133.

Johnson K. T. and Kushiro I. (1992) Segregation of high-pressure partial melts from peridotite using aggregates of diamonds: A new experimental approach. *Geophys. Res. Lett.* **19,** 1703–1706.

Kelemen P. B., Shimizu N., and Dunn T. (1993) Relative depletion of niobium in some arc magmas and the continental crust: Partitioning of K, Nb, La and Ce during melt/rock reaction in the upper mantle. *Earth Planet. Sci. Lett.* **120,** 111–134.

Kelley K. A., Plank T., and Ludden J. N. (2003) The composition of altered oceanic crust at ODP sites 801 and 1149. *Geochem. Geophys. Geosyst.* **4,** 10.1029/2002GC000435.

Kushiro I. (2001) Partial melting experiments on peridotite and origin of mid-ocean ridge basalt. *Annu. Rev. Earth Planet. Sci.* **29,** 71–107.

McDade P., Blundy J., and Wood B. (2003) Trace element partitioning on the Tinaquillo lherzolite solidus at 1.5 GPa. *Am. Mineral.* **88,** 1825–1831.

McDonough W. F. and Frey F. A. (1989) REE in upper mantle rocks. *Geochemistry and Mineralogy of Rare Earth Elements*(eds. B. Lipin and G. R. McKay), pp. 99–145. Rev. Mineral. 21. Mineral. Soc. Am.

McKay G. A. (1989) Partitioning of rare earth elements between silicate minerals and basaltic melts. In *Geochemistry and Mineralogy of Rare Earth Elements*(eds. B. Lipin and G. R. McKay), pp. 45–77. Rev. Mineral. 21. Mineral. Soc. Am.

McKay G. A., Wagstaff J., and Yang S. R. (1986) Clinopyroxene REE distribution coefficients for shergottites: The REE content of Shergotty melt. *Geochim. Cosmochim. Acta* **50,** 927–937.

O'Hara M. J. (1963) Melting of garnet peridotite at 30 kilobars. *Carnegie Inst. Wash. Yearbk.* **62,** 71–76.

Pickering J. M., Schwab B. E., and Johnston A. D. (1998) Off-center hot spots: Double thermocouple determination of the thermal gradient in a 1.27 cm (1/2 in) CaF_2 piston-cylinder furnace assembly. *Am. Mineral.* **83,** 228–235.

Pickering-Witter J. M. and Johnston A. D. (2000) The effect of variable bulk composition on the melting systematics of fertile peridotitic assemblages. *Contrib. Mineral. Petrol.* **140,** 190–211.

Robinson J. A. C., Wood B. J., and Blundy J. D. (1998) The beginning of melting of fertile and depleted peridotite at 1.5 GPa. *Earth Planet. Sci. Lett.* **155,** 97–111.

Salters V. J. M., Longhi J. E., and Bizimis M. (2002) Near mantle solidus trace element partitioning at pressures up to 3.4 GPa. *Geochem. Geophys. Geosys.* **3,** 10.1029/2001GC000148.

Schwab B. E. and Johnston A. D. (2001) Melting systematics of modally variable, compositionally intermediate peridotites and the effects of mineral fertility. *J. Petrol.* **42,** 1789–1811.

Shaw D. M. (1970) Trace element fractionation during anatexis. *Geochim. Cosmochim. Acta* **34,** 237–243.

Sneeringer M. A. and Watson E. B. (1985) Milk cartons and ash cans: Two unconventional welding techniques. *Am. Mineral.* **70,** 200–201.

Stolper E. M. (1980) A phase diagram for mid-ocean ridge basalts: Preliminary results and implications for petrogenesis. *Contrib. Mineral. Petrol.* **74,** 13–27.

Sun S.-S. and McDonough W. F. (1989) Chemical and isotopic systematics of oceanic basalts: Implications for mantle composition and processes. *Magmatism in the Ocean Basins* (eds. A. D. Saunders and M. J. Norry), pp. 313–345. Special Publication 42. Geological Society (London).

Van Orman J. A., Grove T. L., and Shimizu N. (2001) Rare earth element diffusion in diopside: Influence of temperature, pressure, and ionic radius and an elastic model for diffusion in silicates. *Contrib. Mineral. Petrol.* **141,** 687–703.

Wasylenski L. E., Baker M. B., Kent A. J. R., and Stolper E. M. (2003) Near-solidus melting of the shallow upper mentle: Partial melting experiments on depleted peridotites. *J. Petrol.* **44,** 1163–1191.

Watson E. B., Wark D. A., Price J. D., and Van Orman J. A. (2002) Mapping the thermal structure of solid-media pressure assemblies. *Contrib. Mineral. Petrol.* **142,** 640–652.

Wood B. J. and Blundy J. D. (1997) A predictive model for rare earth element partitioning between clinopyroxene and anhydrous silicate melt. *Contrib. Mineral. Petrol.* **129,** 166–181.